Contributions to Mineralogy and Petrology (2021) 176:24
https://doi.org/10.1007/s00410-021-01780-x

ORIGINAL PAPER

What can we learn from REE abundances in clinopyroxene and orthopyroxene in residual mantle peridotites?

Yan Liang[1] · Zejia Ji[1,2] · Boda Liu[1,3]

Received: 12 August 2020 / Accepted: 10 February 2021

Abstract

Clinopyroxene and orthopyroxene are the two major repositories of rare-earth elements (REE) in spinel peridotites. Most geochemical studies of REE in mantle samples focus on clinopyroxene. Recent advances in in situ trace element analysis have made it possible to measure REE abundance in orthopyroxene. The purpose of this study is to determine what additional information one can learn about mantle processes from REE abundances in orthopyroxene coexisting with clinopyroxene in residual spinel peridotites. To address this question, we select a group of spinel peridotite xenoliths (9 samples) and a group of abyssal peridotites (12 samples) that are considered residues of mantle melting and that have major element and REE compositions in the two pyroxenes reported in the literature. We use a disequilibrium double-porosity melting model and the Markov chain Monte Carlo method to invert melting parameters from REE abundance in the bulk sample. We then use a subsolidus reequilibration model to calculate REE redistribution between clinopyroxene and orthopyroxene at the extent of melting inferred from the bulk REE data and at the closure temperature of REE in the two pyroxenes. We compare the calculated results with those observed in clinopyroxene and orthopyroxene in the selected peridotitic samples. Results from our two-step melting followed by subsolidus reequilibration modeling show that it is more reliable to deduce melting parameters from REE abundance in the bulk peridotite than in clinopyroxene. We do not recommend the use of REE in clinopyroxene alone to infer the degree of melting experienced by the mantle xenolith. In general, HREE in clinopyroxene and LREE in orthopyroxene are more susceptible to subsolidus redistribution. The extent of redistribution depends on the modes of clinopyroxene and orthopyroxene in the sample and thermal history experienced by the peridotite. By modeling subsolidus redistribution of REE between orthopyroxene and clinopyroxene after melting, we show that it is possible to discriminate mineral mode of the starting mantle and cooling rate experienced by the peridotitic sample. We conclude that endmembers of the depleted MORB mantle and the primitive mantle are not homogeneous in mineral mode. A modally heterogeneous peridotitic starting mantle provides a simple explanation for the large variations of mineral mode observed in mantle xenoliths and abyssal peridotites. Finally, using different starting mantle compositions in our simulations, we show that composition of the primitive mantle is more suitable for modeling REE depletion in cratonic mantle xenoliths than the composition of the depleted MORB mantle.

Keywords Mantle melting · Disequilibrium melting · Subsolidus reequilibration · REE · Closure temperature · Mantle xenolith · Abyssal peridotite · Orthopyroxene · Clinopyroxene

Communicated by Dante Canil.

✉ Yan Liang
yan_liang@brown.edu

[1] Department of Earth, Environmental and Planetary Sciences, Brown University, Providence, RI 02912, USA

[2] The Key Laboratory of Orogenic Belts and Crustal Evolution, Peking University, Beijing 100871, China

[3] Present Address: Department of Earth, Environmental and Planetary Sciences, Rice University, Houston, TX 77005, USA

Introduction

Rare-earth elements (REE) in mantle rocks have been widely used to study partial melting, melt migration and melt–rock interaction processes in the mantle. Most geochemical studies of REE in spinel peridotites focus on clinopyroxene (cpx) which is the major repository of REE in the peridotites. Important conclusions based on REE abundances in cpx in abyssal peridotites include (1) samples with depleted LREE are resulted from fractional or near fractional melting

Published online: 09 March 2021

(Johnson et al. 1990; Johnson and Dick 1992; Kelemen et al. 1997; Niu and Hékinian 1997; Shimizu 1998; Hellebrand et al. 2001; Brunelli et al. 2006; Liang and Peng 2010; Warren 2016); (2) samples with elevated LREE are affected by melt impregnation and melt–rock interaction (Elthon 1992; Hellebrand et al. 2002; Warren et al. 2009; Brunelli et al. 2014); and (3) cpx with higher HREE but depleted LREE is attributed to fractional melting starting in the garnet stability field (Johnson et al. 1990; Hellebrand et al. 2002; Brunelli et al. 2006). However, not all of the interpretations are unique. For example, the slightly elevated LREE patterns in cpx in abyssal peridotites that show no obvious signs of melt addition can also be explained by small extent of disequilibrium melting (Liang and Liu 2016; Liu and Liang 2017). Near fractional melting starting in the garnet stability field failed to explain some samples with elevated HREE patterns (Liang and Peng 2010). One possible explanation of the higher than expected HREE in residual cpx is subsolidus redistribution (Sun and Liang 2014). During subsolidus reequilibration, REE is strongly and preferentially partitioned into cpx relative to orthopyroxene and olivine in spinel peridotites (e.g., Stosch 1982; Witt-Eickschen and O'Neill 2005; Lee et al. 2007; Liang et al. 2013; Sun and Liang 2014). To sort out the various magmatic and subsolidus processes affecting the abundance and distribution of REE in residual peridotites, additional information is needed.

Recent advances in in situ trace element analysis make it possible to measure REE and other incompatible trace elements in orthopyroxene (opx) with improved precision and confidence. An increasing number of geochemical studies of spinel peridotites have reported REE concentrations in both cpx and opx (e.g., Stosch 1982; Liang and Elthon 1990; McDonough et al. 1992; Rampone et al. 1993; Bedini and Bodinier 1999; Hellebrand et al. 2005; Witt-Eickschen and O'Neill 2005; Warren et al. 2009; Brunelli and Seyler 2010; Seyler et al. 2011; Liu et al. 2012; D'Errico et al. 2016; Quinn et al. 2018). These additional data not only can be used to reconstruct bulk trace element compositions for samples that experienced secondary alteration and to identify samples that were affected by subsolidus reequilibration, but also offer an opportunity for a more complete assessment of the thermal and magmatic history experienced by the peridotite.

The purpose of this study is to determine what more we can learn from REE concentrations in opx in addition to cpx in residual mantle peridotites. To address this question, we use a diffusion-limited disequilibrium double-porosity melting model and a subsolidus reequilibration model to investigate how REE in the bulk residue are fractionated during decompression melting along a mantle adiabat and how REE in residual cpx and opx are redistributed during subsolidus reequilibration after melting. In a closed system, REE abundance in the bulk sample is independent of subsolidus reequilibration, whereas REE abundances in coexisting cpx and opx are sensitive to temperature and mineral mode. Hence, it is more advantageous to infer melting parameters from REE abundance in the bulk sample than in cpx alone. In the absence of chemical disequilibrium, concentrations of REE in opx are related to those in cpx by mineral–melt or mineral–mineral partition coefficients. Hence, REE in residual cpx alone are sufficient for studying the melting history experienced by residual peridotites. This was first demonstrated in the pioneering work of Johnson et al. (1990). However, detailed modeling of REE in residual cpx in abyssal peridotites suggests that their LREE patterns can be better explained if a small extent of chemical disequilibrium is present between cpx and coexisting melt during partial melting (Liang and Liu 2016; Liu and Liang 2017). The present study is built on these recent modeling works by considering REE in opx in addition to cpx during disequilibrium melting. To demonstrate the advantages of the melting followed by subsolidus reequilibration model developed in this study, we conduct two case studies of REE in selected residual spinel peridotites from subcontinental lithosphere (mantle xenoliths) and mid-ocean ridges (abyssal peridotites). We show that this two-step modeling, which has not been done before, allows us to better match the observed REE patterns of cpx and opx in the two sets of peridotite samples. By including REE in opx in our modeling, we can learn not only the melting process but also thermal history experienced by the residual peridotites after melting. The latter is sensitive to mineral modes in the starting mantle. It is possible to constrain mineral mode in the starting mantle and thermal history of the residual peridotites based on REE abundances in both cpx and opx.

Melting followed by subsolidus reequilibration

Model description

We are interested in the fractionation of REE in bulk peridotite during decompression melting in a mantle column and the redistribution of REE between cpx and opx in the peridotite at a subsolidus temperature after melting. We use the disequilibrium double-porosity melting model of Liang and Liu (2016) to simulate REE depletion during decompression melting along a mantle adiabat. For the convenience of a reader, the governing equations are summarized in "Appendix". Key features of the disequilibrium melting model include channelized melt extraction and diffusion-limited chemical exchange between the pyroxenes and the interstitial melt. Since diffusivities of REE in olivine and garnet are considerably larger than those in the pyroxenes

(Van Orman et al. 2001, 2002; Cherniak and Liang 2007; Cherniak 2015) and abundances of REE in olivine and spinel are much smaller than those in the pyroxenes, it is reasonable to assume that olivine and spinel (also garnet for melting in the garnet stability field) are in local chemical equilibrium with their interstitial melt during decompression melting.

There are four dimensionless parameters in the disequilibrium double-porosity melting model for this problem: degree of melting experienced by the residual mantle (F), fraction of melt extracted to the channel ($\mathbb{R}$, called melt suction rate hereafter), disequilibrium parameter of La in cpx ($\varepsilon^{\mathrm{La}}_{\mathrm{cpx}}$), and relative diffusion rate of REE in cpx and opx grains. The degree of melting experienced by a parcel of mantle in an upwelling melting column is defined with respect to the original or starting mantle at the onset of melting by following the advection of the mantle parcel. It is the same as the degree of melting used in the batch or fractional melting model. The melt suction rate is an important parameter of the double-porosity melting model (Iwamori 1994; Lundstrom 2000; Jull et al. 2002; Liang and Peng 2010). The double-porosity model recovers the perfect fractional melting model when $\mathbb{R} = 1$ and the batch melting model when $\mathbb{R} = 0$. We refer the style of melting as near fractional when more than 50% of melt produced by peridotite melting are extracted to the channel ($0.5 < \mathbb{R} < 1$) and near batch melting when less than 50% of melt produced by peridotite melting are extracted to the channel ($0 < \mathbb{R} < 0.5$).

The diffusive exchange rate constants for an REE in opx (R_{opx}) and cpx (R_{cpx}) are inversely proportional to the diffusive time scales for opx and cpx grains (Navon and Stolper 1987; Bodinier et al. 1990; Liang 2003):

$$R_{\mathrm{opx}} = \frac{3\beta D_{\mathrm{opx}}}{d^2_{\mathrm{opx}}} \tag{1a}$$

$$R_{\mathrm{cpx}} = \frac{3\beta D_{\mathrm{cpx}}}{d^2_{\mathrm{cpx}}}, \tag{1b}$$

where D is the diffusion coefficient of REE in opx or cpx; d is the average or effective grain size of opx or cpx; and β is a geometric factor. The relative diffusion rate for an REE is given by the expression:

$$\frac{R^{\mathrm{REE}}_{\mathrm{opx}}}{R^{\mathrm{REE}}_{\mathrm{cpx}}} = \frac{D^{\mathrm{REE}}_{\mathrm{opx}}}{D^{\mathrm{REE}}_{\mathrm{cpx}}} \frac{d^2_{\mathrm{cpx}}}{d^2_{\mathrm{opx}}}. \tag{2}$$

The disequilibrium parameter is a measure of bulk melting rate relative to diffusion rate for the element of interest in a mineral (Eq. 11 in "Appendix"). Given the disequilibrium parameter of La in cpx, disequilibrium parameters for other REE in cpx can be calculated according to their diffusivity ratio (Liang and Liu 2016):

$$\varepsilon^{\mathrm{REE}}_{\mathrm{cpx}} = \frac{D^{\mathrm{La}}_{\mathrm{cpx}}}{D^{\mathrm{REE}}_{\mathrm{cpx}}} \varepsilon^{\mathrm{La}}_{\mathrm{cpx}}. \tag{3}$$

During decompression melting along a mantle adiabat, temperature decreases upward in the melting column. In this study, we calculate the relative diffusion rate and disequilibrium parameters using experimentally determined diffusion parameters for REE in cpx and opx (Van Orman et al. 2001, 2002; Cherniak and Liang 2007). For convenience of numerical calculations, we scale the disequilibrium parameters in Eq. (3) by their respective values at 1300 °C:

$$\varepsilon^{T}_{\mathrm{cpx}} = \frac{D^{1300}_{\mathrm{cpx}}}{D^{T}_{\mathrm{cpx}}} \varepsilon^{1300}_{\mathrm{cpx}}. \tag{4}$$

In the simulations presented below, we treat $\varepsilon^{1300}_{\mathrm{cpx}}$ for La in cpx as a free parameter and calculate the disequilibrium parameter at other temperatures using Eq. (4). Variations of the disequilibrium parameter of La in cpx as a function of temperature and degree of melting along the 1300 °C mantle adiabat can be found in Supplementary Fig. S1. Equilibrium melting is realized when $\varepsilon^{\mathrm{La}}_{\mathrm{cpx}} = 0$.

We use the temperature and major element composition-dependent opx–cpx and olivine–cpx REE partitioning models of Sun and Liang (2014) and mineral mode in the sample to calculate REE abundances in coexisting opx and cpx at a subsolidus temperature after melting. In a closed system, concentration of a trace element in the bulk peridotite (C_{s}) depends on mineral mode and mineral composition, but is independent of temperature, viz.,

$$C_{\mathrm{s}} = w_{\mathrm{cpx}} C_{\mathrm{cpx}} + w_{\mathrm{opx}} C_{\mathrm{opx}} + w_{\mathrm{ol}} C_{\mathrm{ol}} + w_{\mathrm{sp}} C_{\mathrm{sp}}, \tag{5}$$

where w_j and C_j are the weight fraction of and trace element concentration in mineral j in the residual peridotite, respectively. Since REE abundances in olivine and spinel are much lower than those in cpx and opx, concentrations of an REE in cpx and opx at a given temperature (T) can be calculated using the expressions (see also Eq. 18 in "Appendix"):

$$C_{\mathrm{cpx}}(T) = \frac{C_{\mathrm{s}}}{w_{\mathrm{cpx}} + w_{\mathrm{opx}} k_{\mathrm{opx-cpx}}} \tag{6a}$$

$$C_{\mathrm{opx}}(T) = k_{\mathrm{opx-cpx}} C_{\mathrm{cpx}}, \tag{6b}$$

where $k_{\mathrm{opx\text{-}cpx}}$ is the temperature and major element composition-dependent opx–cpx REE partition coefficient. In the case studies presented below, we set the temperature in Eqs. (6a, 6b) to the closure temperature of REE based on the REE-in-two-pyroxene thermometer of Liang et al.

(2013). According to Eqs. (6a, 6b), concentrations of REE in cpx and opx in a residual peridotite vary as a function of mineral mode and temperature even when concentrations of REE in the bulk rock are constant. The sensitivity of REE redistribution to mineral mode and subsolidus temperature will be demonstrated below.

Forward simulations of REE in pyroxenes during melting and subsolidus reequilibration

Variations of REE in opx and cpx in residual peridotites that have experienced decompression melting and subsolidus reequilibration can be visualized through forward simulations using the two-step melting followed by subsolidus reequilibration model outlined in the preceding section. Figure 1a shows one such example for a case of 6% near fractional melting ($\mathbb{R}=0.95$, $\varepsilon_{La}^{1300}=0.01$) of spinel lherzolite along the 1300 °C adiabat. Melting strongly depletes LREE in both cpx and opx, hence, the bulk rock (solid lines in Fig. 1a). Since REE abundances in cpx are considerably higher than those in opx, olivine and spinel, REE pattern of the bulk residue follows that of cpx, forming subparallel trends in the chondrite-normalized REE diagram (Fig. 1a). To the first order, REE abundance in the bulk rock is proportional to the amount of cpx in the residue, viz., $C_s \sim w_{cpx} \times C_{cpx}$. This is demonstrated in Fig. 1a where the abundance of REE in cpx is about 7 times that in the bulk rock and the modal abundance of cpx in the residue after 6% melting is 13.6%. The close similarity between REE in the bulk rock and its constituent cpx forms the basis for using REE in cpx to study mantle-melting processes in the literature.

Figure 1a also shows that REE pattern of residual opx differs considerably from those of cpx and the residue: light and middle REE are preferentially depleted in opx relative to those in the bulk or cpx whereas heavy REE in opx are comparable to those in the bulk rock. This is due to the smaller M2 site of opx structure, making REE more incompatible in opx than in cpx. The net effect is a steeper LREE-depleted pattern for opx in the REE diagram. The REE pattern in opx can be further complicated by subsolidus reequilibration: with decreasing temperature, LREE is preferentially redistributed from opx to cpx, shifting the entire opx REE pattern below that produced by partial melting (cf. dashed and solid green lines in Fig. 1a). Although it is not straightforward to infer melting processes based on REE patterns in opx in residual peridotites that are reset by subsolidus reequilibration, abundances of REE in opx may offer useful information on the thermal history experienced by the peridotite and mineral modes in the starting mantle, as we will demonstrate through two case studies below. However, due to the ionic size-dependent REE opx–cpx partitioning, subsolidus reequilibration mildly elevates HREE in cpx (Fig. 1a, b), which may complicate the interpretation of garnet signature in residual spinel lherzolite and harzburgite (Sun and Liang 2014). Since the abundance of LREE is considerably lower in residual opx, LREE in cpx are not sensitive to subsolidus redistribution in spinel lherzolite. When the degree of melting is large, the modal abundance of cpx decreases in the residue, and the effect of subsolidus reequilibration on the middle and heavy REE in cpx will be more significant. This is illustrated in Fig. 1b for a case of 15% near fractional melting ($\mathbb{R}=0.95$, $\varepsilon_{La}^{1300}=0.01$).

The mineral grain size also affects REE abundances in cpx and opx during disequilibrium melting and subsequent cooling through the relative diffusive exchange rate (Eq. 2). In general, grain size of opx (2–5 mm) is larger than grain size of cpx (<2 mm) in residual spinel peridotites. The effect

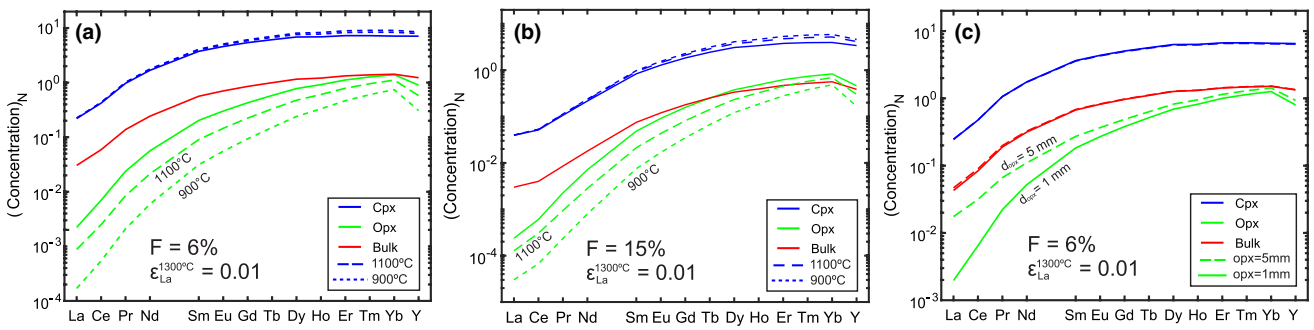

Fig. 1 **a** Forward simulation of REE patterns in residual solid, clinopyroxene (cpx), and orthopyroxene (opx) after 6% disequilibrium melting followed by subsolidus reequilibration. The solid lines represent REE patterns calculated using the disequilibrium melting model and melting parameters of $\varepsilon_{La}^{1300}=0.01$ and $\mathbb{R}=0.95$. The dashed lines represent the recalculated REE concentrations in the two pyroxenes at 1100 °C and 900 °C. **b** Same as **a** but with 15% melting. **c** Comparison of REE patterns in residual solid, cpx, and opx after 6% disequilibrium melting for two choices of opx grain size. The solid lines represent the case of $d_{cpx}=1$ mm and the dashed lines are for $d_{opx}=5$ mm. The grain size of cpx is assumed to be 1 mm. Parameters used in this simulation are as same as in **a**. The temperature-dependent cpx–opx partition coefficients are from Sun and Liang (2014). Concentrations of REE are normalized to CI chondrite using the values of Anders and Grevesse (1989)

of chemical disequilibrium increases with increasing opx grain size, leading to an increase in the effective or apparent partition coefficient for REE between opx and its coexisting melt (Liang and Liu 2016). This can be demonstrated through a forward simulation in which we increase the relative opx-to-cpx grain size from 1 to 5 while keeping the cpx grain size to 1 mm. As shown in Fig. 1c, the calculated middle and heavy REE abundances in cpx slightly decrease whereas the light REE abundances in opx significantly increase compared to the case of 1 mm opx. Consequently, the simulated bulk REE is not very sensitive to the choice of opx/cpx grain size ratio. Regardless of how REE are distributed between opx and cpx by subsolidus reequilibration, the REE abundance in the bulk residue remains the same as that produced by partial melting. Hence, it is more reliable to use REE in the bulk rock to infer melting processes experienced by residual peridotites than REE in cpx alone. We will demonstrate this point through two case studies below.

Applications to residual peridotites

General considerations: data selection, starting mantle composition and mineral mode

We use the two-step melting followed by subsolidus reequilibration model and REE abundances in selected bulk samples and their constituent cpx and opx to infer melting and cooling processes experienced by residual peridotites. For the melting part, we use Bayesian analysis and the disequilibrium double-porosity melting model to invert key melting parameters (F, $\mathbb{R}$, and $\varepsilon^{\mathrm{La}}_{\mathrm{cpx}}$) from the observed REE concentrations in the bulk residual peridotite. Since our inversion is based on bulk REE in the peridotite, REE concentrations in cpx and opx derived from our best-fit model are not required to match the observed REE patterns in cpx and opx in the peridotite sample. For the subsolidus part of our modeling, we use Eqs. (6a, 6b) and the model-predicted bulk REE concentrations from the first step to calculate REE concentrations in cpx and opx at the closure temperature of REE in the two pyroxenes in the peridotite sample. Since subsolidus redistribution of REE between cpx and opx is sensitive to modal abundance (Eqs. 6a, 6b), we carry out the melting and subsolidus redistribution simulations using three choices of starting mantle mode for each sample. Our preferred model produces the closest match to the observed REE concentrations in the bulk rock and the two pyroxenes. "Appendix" summarizes the governing equations and the inversion method.

To demonstrate the advantages of the two-step modeling, we model REE + Y abundances in selected residual spinel peridotite samples from subcontinental lithosphere (mantle xenoliths, nine samples) and suboceanic lithosphere (abyssal peridotites, 12 samples). We include Y in our analysis because it behaves similarly to HREE during mantle melting and its abundance is routinely reported along with REE in opx and cpx. Peridotites from subcontinental and suboceanic lithospheres have different thermal history. Peridotites from stable cratons are generally well equilibrated and have similar and relatively low equilibrium or closure temperatures for both major elements and REE in coexisting cpx and opx, whereas abyssal peridotites have higher closure temperatures for REE than major elements in pyroxenes (Liang et al. 2013; Dygert and Liang 2015; Wang et al. 2015). This is illustrated in Fig. 2 for the selected samples in this study. Since abyssal peridotites are variously serpentinized and some mantle xenoliths contain glass veins, we use measured REE + Y abundances in minerals (cpx, opx, and olivine when available) and mineral modes reported in the literature to reconstruct bulk REE + Y abundances in the peridotites. As shown in Fig. 1, the light and middle REE in opx are considerably lower than those in cpx, making accurate measurements of these elements in opx an analytical challenge. This problem is especially prevalent for odd atomic number elements such as La (57) and Pr (59), resulting in scattered LREE patterns in some samples. To include more elements and more samples in this study, we applied an interpolation/extrapolation procedure to some of the samples that exhibit scattered REE patterns. The procedure, detailed in Supplementary Materials (*REE interpolation procedure and*

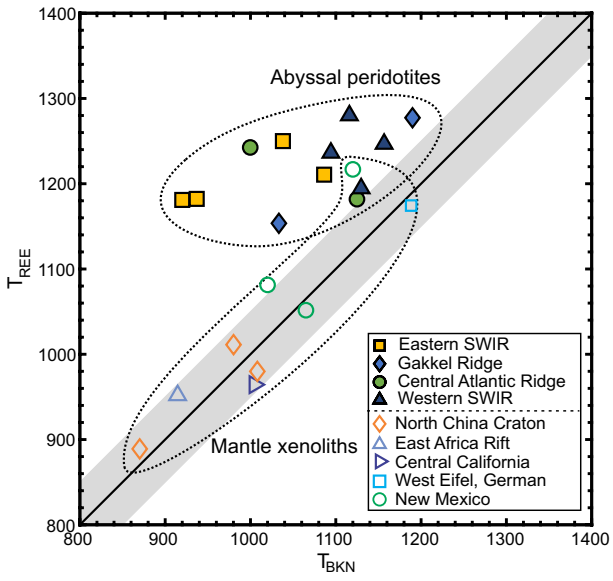

Fig. 2 Comparison of the temperatures derived from the REE-in-two-pyroxene thermometer of Liang et al. (2013, T_{REE}) and those calculated using the two-pyroxene thermometer of Brey and Köhler (1990, T_{BKN}) for the 9 mantle xenoliths and 12 abyssal peridotites included in this study (see text for a list of the source of data). All calculations were performed assuming a pressure of 1.5 GPa

results), is based on correlation between the nearest neighbor REE (e.g., La and Ce) established by mantle pyroxenes that have smooth REE patterns. In Supplementary Table S1a, we list mineral modes and REE concentrations in cpx, opx, and the bulk peridotite included in this study.

To use the disequilibrium melting model, we need to know mineral grain size, mineral mode, and composition of the starting mantle. Following standard practice in REE modeling, we assume that abundances of REE + Y in the starting mantle are the same as the average depleted MORB mantle (DMM, Workman and Hart 2005) for abyssal peridotites and the primitive mantle (PM, McDonough and Sun 1995) for mantle xenoliths in our first round of simulations. To assess uncertainties and misfits, we also explore other starting mantle compositions. The mineralogy of the starting mantle is a primitive spinel or garnet lherzolite. There are some uncertainties in the mineral mode of the starting mantle. For example, the DMM of Workman and Hart (2005) consists of 13% cpx, 28% opx, 57% olivine, and 2% spinel, whereas the starting mantle of Johnson (1998) and Hellebrand et al. (2002) has 17% cpx, 27% opx, 53% olivine, and 3% spinel. The latter has been used in our inverse modeling of REE depletion in residual cpx from abyssal peridotites (Liang and Peng 2010; Liang and Liu 2016; Liu and Liang 2017). Figure 3a, b shows large variations in mineral modes in both mantle xenoliths and abyssal peridotites. [For more peridotite data, a reader is referred to Fig. 1 in Bodinier and Godard (2014) and Fig. 4 in Warren (2016).] Even for the small number of samples included in the present study, the range of modal variations cannot be explained by a single melting trend or melting reaction using either aforementioned starting mode. It is possible that mineral modes are not well constrained for some of the peridotite samples (e.g., heavily serpentinized abyssal peridotites). It is also possible that mineral mode in the starting mantle is not uniform, considering the efficiency of mantle convection, lithological heterogeneities in the mantle, and diversity of peridotites in the field. In this study, we consider three mineral modes for the starting mantle source. To reduce the number of free parameters in our modeling, we fix the modal abundance of olivine in the mantle source to 56% or 60.5% and vary the cpx:opx proportion in the mantle source for the mantle xenolith or abyssal peridotite samples (Fig. 3a, b). This is a reasonable approach as (1) the relative REE pattern in the bulk rock is not very sensitive to the abundance of olivine in the mantle source, and (2) the resultant residual modes cover a wide range of mineral modal abundances (Fig. 3). Finally, the grain size of the starting mantle is unknown, although in general grain size of opx is larger than grain size of cpx in peridotites. As a starting model, we assume that the grain size ratio between opx and cpx does not change during melting. The latter helps to simplify the evaluation of the relative diffusion rate between opx and cpx (Eq. 2).

Case study 1: mantle xenoliths

To demonstrate the basic features of the disequilibrium melting model and the effect of subsolidus redistribution, we select nine well-characterized spinel lherzolite and harzburgite xenoliths from the literature: three samples from Yangyuan, North China Craton (Liu et al. 2012), one sample from West Eifel, Germany (Witt-Eickschen and O'Neill 2005), one sample from East Africa Rift (Bedini and Bodinier 1999), three samples from Kilbourne Hole, New Mexico (Harvey et al. 2012), and one sample from the Coast Ranges of central California (Quinn et al. 2018). These samples are protogranular, free of garnet, plagioclase, hydrous minerals and veins. They are selected on the basis of their depleted light REE patterns in cpx and opx, well-defined linear trends for at least the middle and HREE in the inversion diagram of the REE-in-two-pyroxene thermometer, and similar equilibrium temperatures between major element-based and REE-based pyroxene thermometers. Figure 2 shows that the calculated temperatures are well below

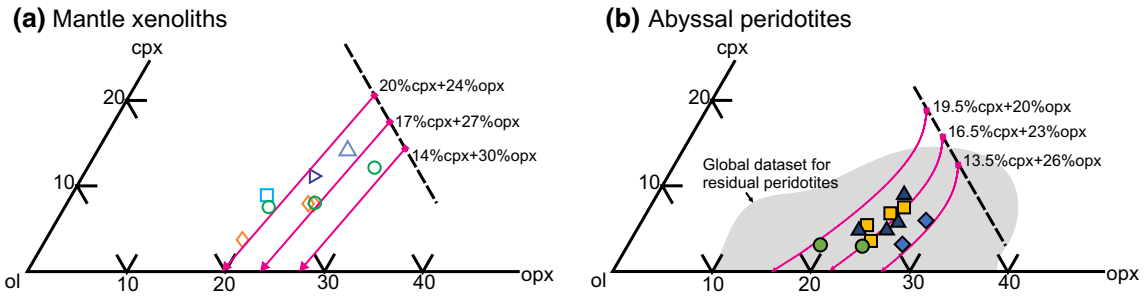

Fig. 3 Modal abundances of clinopyroxene (cpx), orthopyroxene (opx), and olivine (ol) in mantle xenoliths (**a**) and abyssal peridotites (**b**) selected in this study. The magenta lines in **a** are calculated using the melting reaction of Baker and Stolper (1994): 0.38 opx + 0.71 cpx + 0.13 spinel = 0.22 olivine + 1 melt and for three choices of starting mantle mode. The light grey area in **b** is based on Warren (2016) for residual abyssal peridotites from around the world. The magenta curves in **b** represent melting paths based on pMELTS with potential temperature of 1330 °C and 150 ppm water content and three choices of starting mantle mode. Sample legends are the same as in Fig. 2

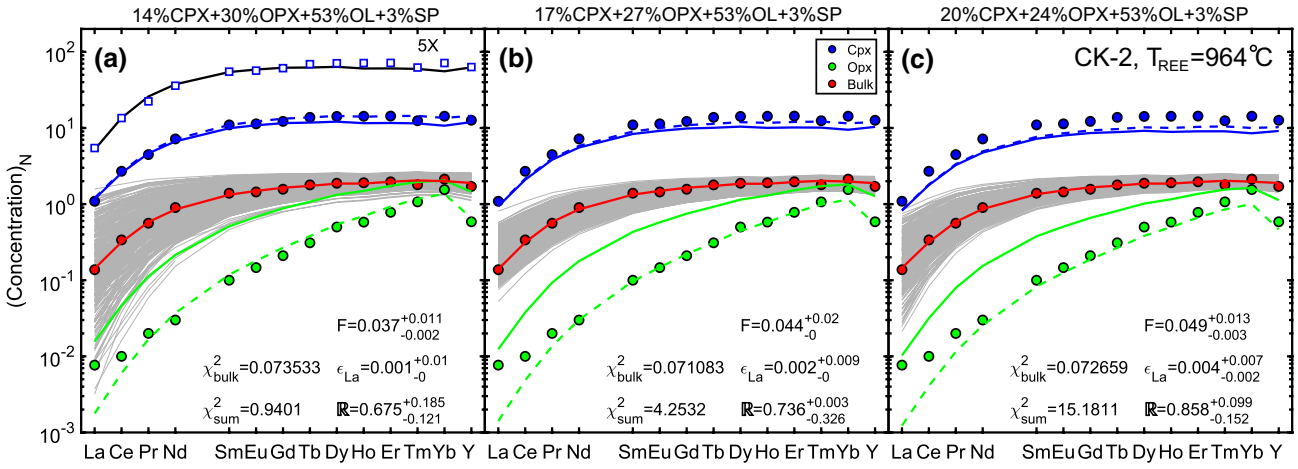

Fig. 4 Comparison between observed (circles) and model-derived (curves) REE + Y patterns in the bulk and two pyroxenes in the xenolith sample CK-2 (Quinn et al. 2018). Simulation results for three starting mantle modes are shown in **a**–**c**. The grey solid curves are MCMC predictions and the red solid curve represents the best-fit of the bulk REE + Y data. The solid blue and green curves represent the calculated REE abundances in cpx and opx, respectively, based on the inverted melting parameters of the best-fit of the bulk data. The dashed blue and green curves represent the model-predicted subsolidus REE abundances in cpx and opx at $T = T_{\mathrm{REE}}$, calculated using the temperature-dependent cpx–opx partition coefficients of Sun and Liang (2014). The sum of Pearson's Chi-square (χ^2_{sum}) is the sum of the Chi-squares of simulated bulk (red curve) and simulated cpx and opx after subsolidus re-equilibrium (dashed bulk and green curves). The open squares and black curve in **a** represent the cpx data and the best-fit result based on the cpx-alone melting model. For clarity, data from cpx-alone simulations were elevated by a factor of 5. Concentrations of REE are normalized to CI chondrite using the values of Anders and Grevesse (1989)

the solidus of the peridotite xenoliths. Figure 3a displays modal abundances of the selected samples. Figure 4 shows an example of MCMC simulations for sample CK-2 from the Coast Ranges of central California (Quinn et al. 2018). Figure 5 presents the best-fit models for the nine xenoliths with PM starting compositions. For reference, we plot selected major element concentrations in these samples as a function of bulk MgO and spinel Cr# (= 100Cr/Cr + Al, in molar) in Supplementary Figs. S2a and S2b. Supplementary Tables S1b and S2 and Fig. S4 present results of MCMC simulations with PM and DMM starting compositions and three choices of starting mantle mode for the nine xenolith samples along the 1300 °C mantle adiabat (Fig. S1). In this first application, we use the melting reaction of Baker and Stolper (1994) for spinel lherzolite in our melting model. The main results are summarized below.

First, the bulk REE patterns are well reproduced by the disequilibrium double-porosity melting model. The quality of fit is not very sensitive to the choice of starting mantle mode (cf. Fig. 4a–c). This is shown by the similar Pearson's Chi-squares among the three cases for each sample (Supplementary Table S2). Here, we calculate Pearson's Chi-square for the bulk REE after inversion using the expression:

$$\chi^2_{\mathrm{bulk}} = \sum_{j=1}^{N} \frac{\left(C_{s,j} - C^{\mathrm{m}}_{s,j}\right)^2}{C_{s,j}}, \tag{7}$$

where $C_{s,j}$ and $C^{\mathrm{m}}_{s,j}$ are the model-derived and measured bulk solid concentrations for element j, respectively; N (= 14) is the number of elements in the model. In general, the smaller the Pearson's Chi-square, the better the model prediction will be. There is a small trade-off between cpx abundance in the starting mantle and the degree of melting: the higher the cpx mode in the starting mantle, the greater the degree of melting is required to match the observed depletion in REE in the bulk residue. Increasing cpx mode from 14 to 20% in the starting mantle results in 0.11–3% increase in the inferred degree of melting for the nine xenolith samples.

Second, the observed REE patterns in residual cpx and opx (filled blue and green circles in Figs. 4, 5) cannot be reproduced directly using melting parameters derived from the bulk REE pattern (blue and green solid lines). Very often, LREE in opx is overestimated and HREE in cpx is underestimated by the melting model, which appears to be consistent with the subsolidus reequilibration trends displayed in Fig. 1. To quantify the effect of subsolidus redistribution, we recalculate the model-derived REE concentrations in opx and cpx using the temperature and major element composition-dependent REE opx–cpx partition coefficients (Sun and Liang 2014) and closure temperatures (T_{REE}) derived from the REE-in-two-pyroxene thermometer (Liang et al. 2013). The latter is 964 °C for sample CK-2. Figures 4 and 5 (see also Supplementary Fig. S4) show that the matches to the measured REE patterns in cpx and opx in

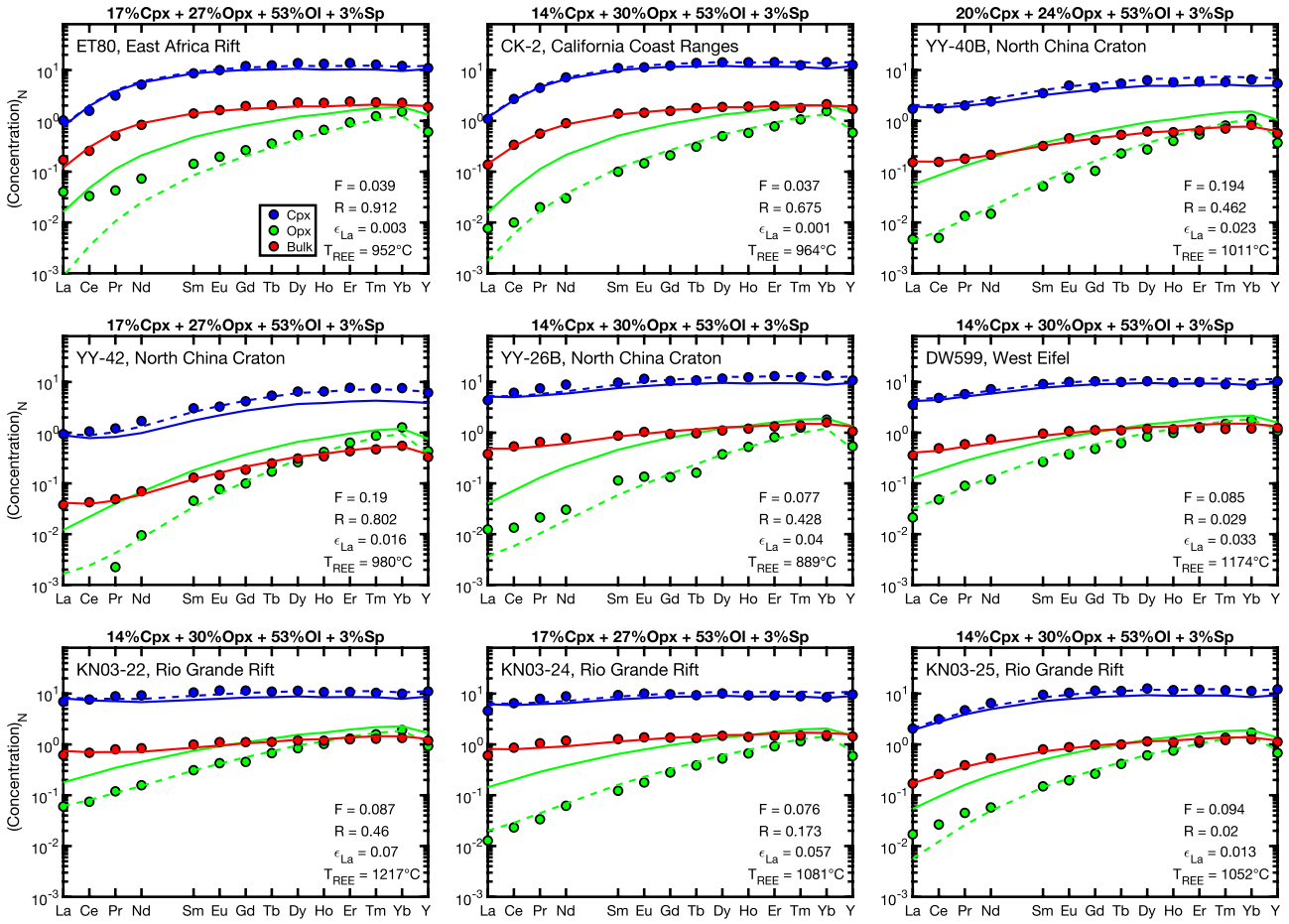

Fig. 5 Summary of preferred models for the nine mantle xenolith samples with REE + Y in the primitive mantle as starting mantle compositions. Modal abundance of the starting mantle is listed for each sample. The solid red curves are the best-fits of the bulk REE + Y data (circles). The solid blue and green curves represent the calculated REE concentrations in cpx and opx, respectively, based on the inverted melting parameters. The dashed blue and green curves represent the model-predicted subsolidus REE abundances in cpx and opx at $T = T_{REE}$, calculated using the temperature-dependent cpx–opx partition coefficients of Sun and Liang (2014). Results of MCMC simulations with PM and DMM starting compositions for the nine xenolith samples are presented in Supplementary Fig. S4 and Tables S1b and S2

the nine xenolith samples are considerably improved after adjustment of subsolidus redistribution (dashed lines).

Finally, for a given sample, our preferred starting mantle mode and melting parameter should have the smallest sum of Pearson's Chi-squares for the bulk peridotite, cpx, and opx among the three starting mantle modes, where Pearson's Chi-squares for cpx and opx are calculated after adjustment for subsolidus reequilibration. Figure 5 summaries results of our preferred model and Supplementary Table S2 provides additional information on uncertainties of our preferred melting parameters and Pearson's Chi-squares. To facilitate discussion, we also invert melting parameters from REE in cpx alone using the disequilibrium melting model of Liu and Liang (2017). It is interesting to note that the quality of fit to REE patterns in cpx is comparable to that based on inversion of REE in cpx alone, as the calculated Pearson's Chi-squares for cpx from the bulk model and cpx alone model are very similar for the nine samples (Supplementary Table S2). The misfits, if present, are mostly LREE in opx and cpx. Figure 4 and Supplementary Fig. S4 also show that the recalculated REE patterns in model-derived opx and cpx (dashed lines) are sensitive to starting mantle mode. This is highlighted by the large differences in the sum of Pearson's Chi-squares among the three choices of mantle mode (e.g., 0.94, 4.25, and 15.2 for 14%, 17%, and 20% cpx in the starting mantle, respectively for sample CK-2). Hence, by modeling REE redistribution among cpx, opx, and olivine in the residual mantle xenolith after melting, it is possible to constrain mineral mode of the starting mantle. Preferred mineral modes in the starting mantle for the nine xenoliths are listed in Fig. 5.

Case study 2: abyssal peridotites

To critically assess the roles of garnet field melting, finite rate of chemical exchange for LREE fractionation in cpx, and subsolidus redistribution of REE between cpx and opx in affecting REE patterns in abyssal peridotites, we select 12 residual abyssal peridotites from the literature that reported REE abundances in both cpx and opx: four samples from eastern Southwest Indian Ridge (SWIR, Seyler et al. 2011), two samples from Gakkel Ridge (D'Errico et al. 2016), four samples from western SWIR (Warren et al. 2009), and two samples from Central Atlantic Ridge (Brunelli and Seyler 2010). Based on the criteria of Warren (2016), these samples are residual peridotites as they are free of plagioclase and melt veins, have low TiO_2 in spinel and depleted LREE patterns in cpx and opx. Similar to mantle xenoliths, these samples also have well-defined linear trends for at least the middle and heavy REE in the inversion diagram of the REE-in-two-pyroxene thermometer. Figure 3b displays modal abundances of the selected samples. For reference, we also plot major element compositions of the samples as a function of bulk MgO content and spinel Cr# in Supplementary Figs. S3a and S3b.

The extent of melting in the garnet stability field is a free parameter in most geochemical studies of REE fractionation during garnet peridotite melting, with values ranging from less than 1% to more than 10% (e.g., Johnson et al. 1990; Hellebrand et al. 2002; Brunelli et al. 2006; Liang and Peng 2010). This free parameter can be eliminated by considering the thermodynamics of peridotite melting. In this study, we use pMELTS (Ghiorso et al. 2002) to calculate mineral mode along an adiabatic melting path that has a potential temperature of 1330 ℃. The starting mantle (DMM) contains 150 ppm water and melting starts in the garnet stability field. In this pMELTS-based model, the maximum extent of melting in the garnet stability field is 0.7% and the cpx exhausts at $F = 20\%$. There is neither clear experimental nor geophysical evidence for the presence of high-porosity channels at depth greater than 60 km beneath mid-ocean ridges. Based on 2D double-porosity ridge modeling, Liu and Liang (2019) suggest that high-porosity channels initiating at depth less than 60 km can better explain geophysically inferred high-porosity region beneath the ridge axis (Yang et al. 2007; Key et al. 2013). In the absence of high-porosity channels, the melt suction rate reduces to zero in the double-porosity model (i.e., $\mathbb{R} = 0$). For this reason, we use batch melting to model decompression melting in the garnet stability field for abyssal peridotites. Figure 3b displays variations of mineral mode in residual peridotites calculated using pMELTS for three choices of starting mantle mode (solid curves). These residual trends bracket the observed modal variations in the selected samples. The pMELTS-derived mineral modes vary somewhat nonlinearly as a function of F. Nonetheless, the average melting reaction derived from the pMELTS-based modeling is very similar to the 1 GPa melting reactions of Baker and Stolper (1994) and Kinzler and Grove (1992) for spinel lherzolite (see Table 2 in Walter 2014). Figure 6 shows an example of MCMC simulations for sample Van 7-85-49 from Western SWIR (Warren et al. 2009). Figure 7 summaries results of our preferred model for the 12 abyssal peridotite samples. Supplementary Fig. S5 presents detailed simulation results for individual samples. Supplementary Tables S1c and S2 provide additional information on uncertainties of our preferred melting parameters, Pearson's Chi-squares, and results from cpx alone inversion. The main results are summarized below.

Similar to the case of mantle xenolith, the disequilibrium double-porosity melting model can fit the bulk REE patterns

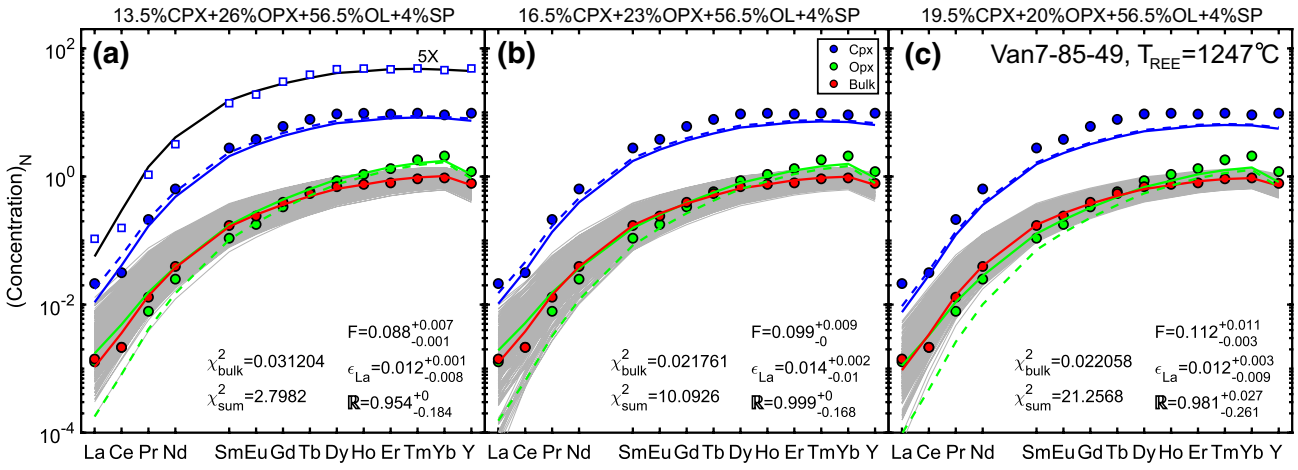

Fig. 6 Comparison between observed (circles) and model-derived (curves) REE + Y patterns in the bulk and two pyroxenes in the abyssal peridotite sample Van7-85-49 (Warren et al. 2009). For a detailed explanation of symbols and curves, a reader is referred to the caption to Fig. 4

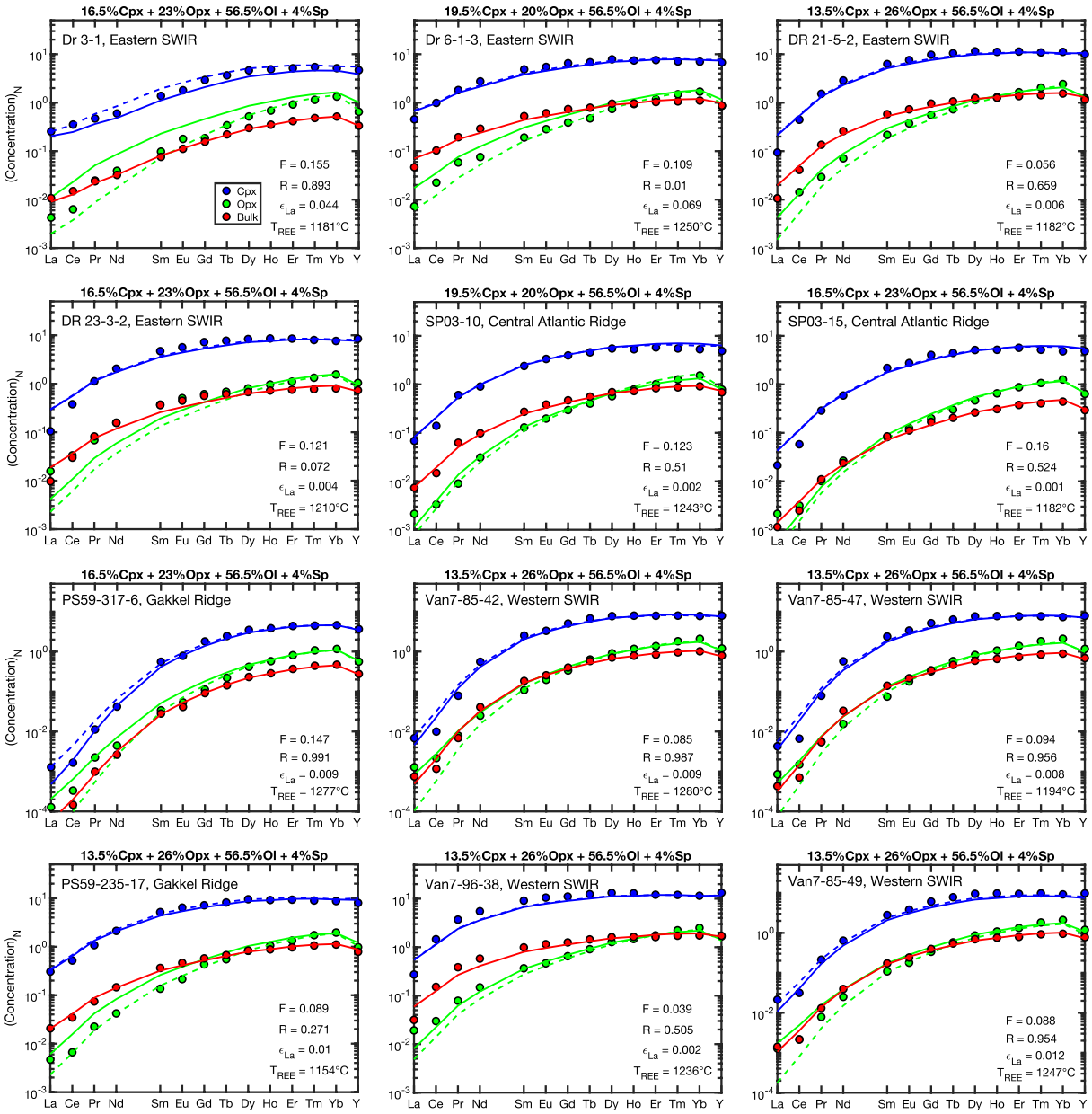

Fig. 7 Summary of preferred models for the 12 abyssal peridotite samples with REE + Y in DMM as starting mantle compositions. Modal abundance of the starting mantle is listed for each sample. Supplementary Fig. S5 presents detailed simulation results for individual samples. Supplementary Tables S1c and S2 provide additional information on uncertainties of preferred melting parameters, Pearson's Chi-squares, and results from cpx alone inversion. Symbols are the same as those described in the caption to Fig. 5

very well for most of the abyssal peridotite samples included in this study (Fig. 7). The exceptions are sample Van7-96-38 from Western SWIR (Warren et al. 2009) and sample Dr 23-3-2 from Eastern SWIR (Seyler et al. 2011) which exhibit some misfits in light and middle REE (Figs. 7, S5). As in the case of mantle xenolith, the quality of fit to the bulk REE data is not very sensitive to the starting mantle mode, whereas the match to the measured REE in cpx and opx depends strongly on the starting mantle mode (cf. the three cases in Fig. 6, for other samples see Fig. S5). Overall, the matches to the observed REE patterns in cpx and opx are improved after adjustment of subsolidus redistribution (cf. solid and dashed lines in Fig. 7). However, the improvement is moderate because of the relatively high T_{REE} for the peridotite samples and very small adjustment for REE in cpx. This may result from incomplete reequilibration of REE between cpx and opx, as we discuss below. Supplementary Table 2 lists melting parameters of our preferred model for the 12 abyssal peridotite samples based on the sum of

Pearson's Chi-squares of the bulk and the two pyroxenes calculated after adjustment for subsolidus reequilibration.

Discussion

Misfits of REE in the bulk samples

Although the disequilibrium double-porosity melting model can account for most of the variations of REE + Y in the bulk peridotites, noticeable misfits in the light and middle REE are observed in samples Van7-96-38 (from Western SWIR, Warren et al. 2009) and Dr23-3-2 (from eastern SWIR, Seyler et al. 2011, see Figs. 7, S5). In both cases, the model-predicted La, Er, Tm and Yb in the bulk residue are higher than, whereas the predicted Nd, Sm, E, Gd and Tb are lower than, measured values in the samples. This humped feature is not sensitive to starting mantle mode, and is also present in the cpx-alone inversion models. Addition of melt would elevate La in cpx and opx and hence, cannot explain the depleted LREE patterns in the two samples. The lower than expected bulk La, Er, Tm and Yb can be accounted for by increasing the degree of melting, but this would result in additional misfits in Nd, Sm, E, Gd and Tb. Since partition coefficients of middle REE in cpx are higher than those in garnet and the partition coefficients of HREE in cpx are lower than those in garnet, prolonged melting in the garnet stability field can produce the humped middle REE pattern in cpx and the bulk residue (e.g., Johnson et al. 1990). Our pMELTS-based model for abyssal peridotites includes 0.7% initial melting in the garnet field. To further explore the role of garnet field melting, we consider a hypothetic case in which batch melting in the garnet stability field is 4.1%. Supplementary Fig. S6 presents the simulation results. The simulated bulk rock and pyroxene REE patterns after 4.1% batch melting in the garnet field show only a small improvement for sample Dr23-3-2 (the sum of Pearson's Chi-squares decreases from 3.8 to 3.3 which is still higher than the other ten abyssal peridotites) and no improvement at all for sample Van7-96-38. Hence, the misfits are unlikely due to batch melting in the garnet stability field. Although fractional melting of garnet lherzolite can produce humped REE pattern in cpx (Johnson et al. 1990), the physical mechanism for fractional melting in the garnet stability field remains uncertain.

Abyssal peridotites are heavily altered by serpentinization. It is possible that mineral modes in these two samples are not accurately determined. To explore this possibility, we reconstruct two new modal abundances for the two samples: one by increasing cpx mode by 2% and decreasing opx mode by 2%, and the other by decreasing cpx mode by 2% and increasing opx mode by 2%. We run MCMC simulations followed by subsolidus redistribution for these four cases and the results are shown in Supplementary Fig. S7. Changing cpx mode by ± 2% in the samples does not lead to a significant improvement in the fit to the reconstructed bulk REE in these two samples (i.e., the humped pattern persists). However, addition of 2% cpx does result in moderate improvement in the match to the observed REE patterns

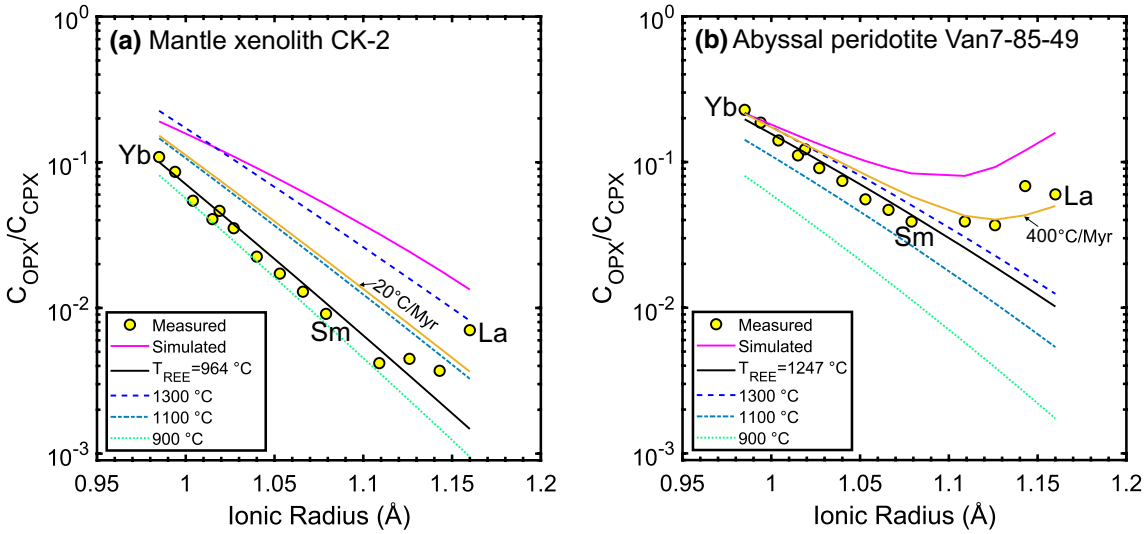

Fig. 8 Variations of the apparent opx–cpx REE partition coefficient as a function of REE ionic radius for the xenolith sample CK-2 (**a**) and abyssal peridotite Van7-85-49 (**b**). The yellow circles represent the measured data. The magenta and black curves represent the model-predicted apparent partition coefficients at the end of melting and at the subsolidus temperature $T = T_{REE}$, respectively. The thin orange curves were calculated using a simple model for diffusive reequilibration between two minerals at the stated cooling rates. The three dashed curves are the calculated opx–cpx REE partition coefficients using the model of Sun and Liang (2014)

in cpx and opx in the two samples. This is confirmed by the smaller sum of Pearson's Chi-squares for the + 2% cpx case.

We should point out that none of the hypotheses explored in this section can explain the humped REE pattern in cpx using the cpx-alone inversion model. In theory, one can match the observed REE pattern in bulk residue by judiciously adjusting starting mantle composition. It is possible that composition of the starting mantle for these two samples are different from DMM.

Partition of REE between opx and cpx: incomplete reequilibration?

A common misfit shared by all the abyssal peridotite samples and four of the nine mantle xenoliths (ET80, CK-2, YY-26B, and KN03-25) in this study is that model-derived LREE in opx are lower than measured values even after adjustment of subsolidus redistribution. The misfit can be visualized by plotting the apparent opx/cpx REE partition coefficient against REE ionic radius: the apparent partition coefficients for the middle and heavy REE follow closely to an isotherm, whereas those for LREE are gradually displaced above the isotherm, defining a spoon-shaped or U-shaped pattern (Fig. 8a, b). In the inversion diagram for the REE-in-two-pyroxene thermometer, the displaced LREE fall below the linear trend established by the heavy and middle REE and are excluded from the temperature calculation (Liang et al. 2013). Spoon- or U-shaped opx/cpx REE partitioning pattern is a common feature among mantle samples (e.g., Stosch 1982; Agranier and Lee 2007; Seyler et al. 2011). It arises when LREE in opx and cpx are out of chemical equilibrium. Agranier and Lee (2007) identified two mechanisms that can produce U-shaped disequilibrium patterns in mantle xenoliths from Dish Hill, California and abyssal peridotites from the Gakkel Ridge: diffusive fractionation at subsolidus state or metasomatism introduced by "injection and subsequent freezing in of small amounts of melt" under lithospheric or asthenospheric conditions. The nine mantle xenoliths and twelve abyssal peridotite samples included in the present study are all depleted in LREE. Given that our disequilibrium double-porosity melting model can reproduce the bulk REE patterns very well in these samples, we can rule out the recent melt addition hypothesis for these samples.

We suggest that the spoon- or U-shaped opx/cpx REE partitioning patterns can be produced by disequilibrium melting followed by diffusive exchange between cpx and opx at subsolidus state. Figure 8a, b compares the apparent opx/cpx REE partition coefficients calculated from the measured REE abundances in opx and cpx in mantle xenolith CK-2 from the Coast Ranges of central California (Quinn et al. 2018, filled circles) and abyssal peridotite Van7-85-49 from western SWIR (Warren et al. 2009) with those calculated using melting parameters derived from our MCMC simulations (magenta lines). (Similar plots for other samples included in this study are presented in Supplementary Figs. S4, S5.) As shown in Fig. 8a, b, the simulated apparent partition coefficients at the end of melting are displaced above the measured values. Since opx/cpx REE partition coefficients decrease with the decrease of temperature (cf. the three isotherms in Fig. 8) and diffusion coefficients of REE in cpx increase systematically from La to Lu at a given temperature (Van Orman et al. 2001, 2002; see also Supplementary Fig. S1c), time scales for diffusive exchange between opx and cpx in a closed system are longer for LREE than HREE (see Fig. 5 in Liang 2014). During diffusive reequilibration, HREE approach opx/cpx equilibrium partitioning faster than LREE. Depending on thermal history experienced by the samples (e.g., cooling and upwelling rates), the elevated opx/cpx REE patterns produced by disequilibrium melting (magenta lines in Fig. 8) would be gradually relaxed to the spoon-shaped pattern recorded in the peridotite samples (filled circles). As a proof-of-concept, we carry out two forward simulations of diffusive reequilibration of REE between opx and cpx under two prescribed cooling rates. In this simple demonstration, cooling starts at the end of melting and terminates at the closure temperature of REE (i.e., $T = T_{REE}$). Figure 8a, b shows that the results are promising (orange curves). In a more realistic situation, the cooling rate, which is likely very different for the mantle xenolith and abyssal peridotite, may vary as a function of time. Hence, it may be possible to deduce cooling rate through detailed modeling of the spoon-shaped opx/cpx REE patterns in residual peridotites, a subject we will pursue in the future.

Mantle source composition

The starting mantle composition (DMM vs. PM) affects our inversion results. The depleted MORB mantle or DMM has been widely used in REE modeling of abyssal peridotites. In their original studies of mantle xenoliths, Liu et al. (2012) and Harvey et al. (2012) anchored their major and trace element data to the primitive mantle of McDonough and Sun (1995), whereas Quinn et al (2018) used HREE in their samples and DMM of Workman and Hart (2005) to infer the extent of melting. We used the primitive mantle of McDonough and Sun (1995) as the starting mantle composition in our inversion of the mantle xenolith data (Fig. 5). Composition of the mantle source is unlikely homogeneous, even for a suite of depleted samples from the same locality. Liu et al. (2012) reported Nd and Hf isotopic compositions of cpx for the three North China Craton samples (YY-26, YY-40B, and YY-42) included in this study. They found that samples YY-40B and YY-42 have considerably higher $^{143}Nd/^{144}Nd$ and $^{176}Hf/^{177}Hf$ ratios than sample YY-26 and suggested that

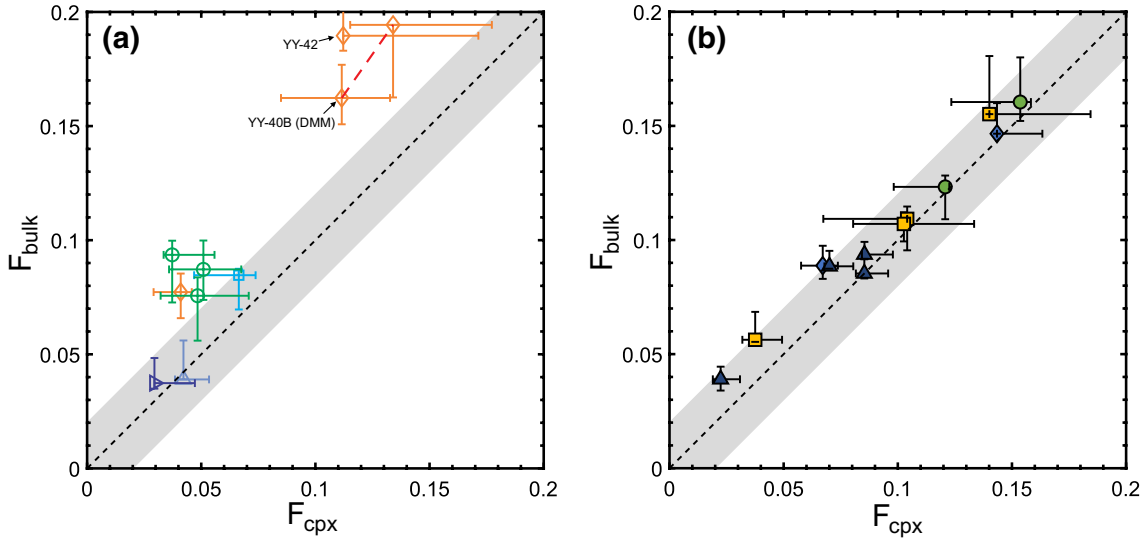

Fig. 9 Comparison of the degree of melting derived from the cpx-alone inversion (F_{cpx}) and the degree of melting derived from inversion of the bulk sample (F_{bulk}) for the mantle xenoliths (**a**) and abyssal peridotites (**b**) selected in this study. The dashed lines and grey areas represent the 1:1 ratio within ±2% range. The red dashed line in **a** connects the inversion results of sample YY-40B with primitive mantle (PM) and the depleted MORB mantle (DMM) starting compositions. Error bars are based on MCMC simulations. Sample legends are the same as in Fig. 2

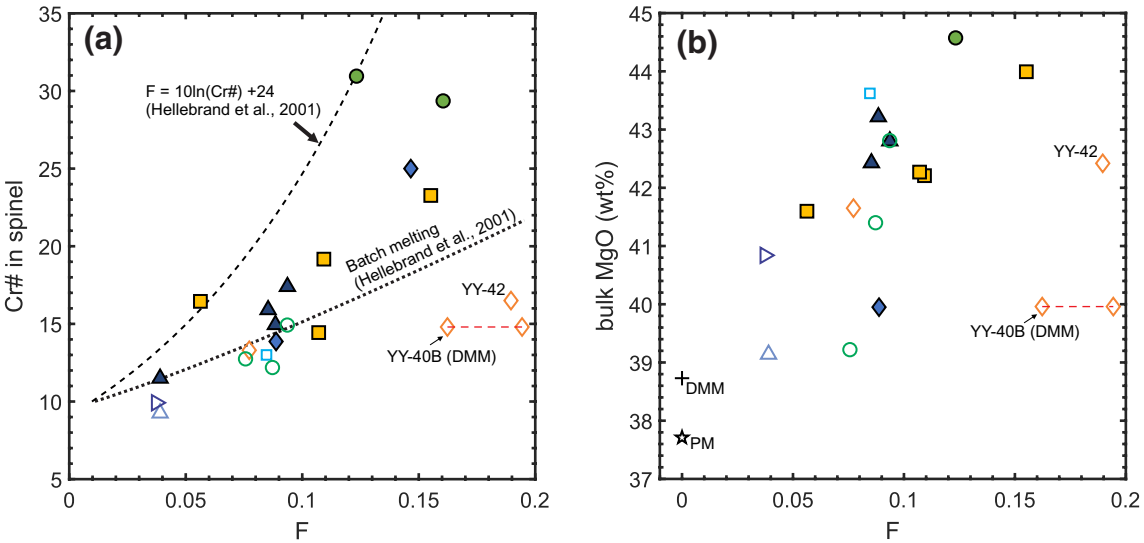

Fig. 10 Variations of spinel Cr# (**a**) and bulk MgO content (**b**) as a function of the degree of melting for the mantle xenoliths (open symbols) and abyssal peridotites (filled symbols) included in this study. The two dashed lines are based on the empirical expressions of Hellebrand et al. (2001) for fractional and batch melting. Symbols are the same as in Fig. 2

samples such as YY-26 might be affected by melt addition via melt–rock interaction. As shown in Fig. 5, REE patterns in the bulk sample, cpx, and opx in YY-26 can be well reproduced by our two-step model using PM as the starting mantle composition (see also Fig. S4). The less depleted LREE in cpx and the bulk peridotite (also samples DW599, KN03-22 and KN03-24 in Fig. 5) result from a combination of greater role of batch melting ($\mathbb{R} < 0.5$) and larger extent of chemical disequilibrium ($\varepsilon_{La} \sim 0.03$–$0.07$), both hinders the depletion of LREE during peridotite melting. The higher $^{143}Nd/^{144}Nd$ and $^{176}Hf/^{177}Hf$ ratios in samples YY-40B and YY-42 suggest that these samples may have derived from a more depleted mantle source. To test this hypothesis, we run MCMC simulations for samples YY-40B and YY-42 using DMM as our starting mantle composition. The results are summarized in Supplementary Table S2 and Fig. S4:

the fits to sample YY-40B are slightly improved as the sum of Pearson's Chi-squares decreases from 1.76 (PM) to 1.68 (DMM), whereas no improvement is observed for YY-42 as the sum of Pearson's Chi-squares increases from 0.62 (PM) to 1.21 (DMM). In fact, inversion of the remaining seven xenolith samples with DMM starting composition leads to moderate to significant reduction in the quality of fits to the observed REE patterns (i.e., the sum of Pearson's Chi-squares has increased, Fig. S4). This intriguing result suggests that composition of PM is more suitable for modeling REE depletion in the nine residual mantle xenoliths included in this study. Given the slight improvement of fits to sample YY-40B using DMM starting mantle composition, we include inversion results with DMM starting composition in our discussion (two points connected by red dashed lines in Figs. 9a, 10 below).

Composition of the average DMM is a convenient common starting point in modeling REE depletion in abyssal peridotites. According to Warren et al. (2009), $^{143}Nd/^{144}Nd$ ratios in cpx in the four samples from SWIR (Van7-85-42, Van7-85-47, Van7-85-49, and Van7-96-38) are more similar to the depleted endmember of DMM (D-DMM) of Workman and Hart (2005) than the average DMM (see Fig. 5a in Warren et al. 2009). Intrigued, we ran MCMC simulations again for the four samples using REE + Y in the D-DMM of Workman and Hart (2005) as the starting mantle composition. The results are presented in Supplementary Fig. S8: the fits to the observed REE in the bulk, cpx, and opx are slightly improved as the sums of Pearson's Chi-squares for the four samples are all reduced. The small improvement is probably due to the fact that concentration differences between D-DMM and DMM of Workman and Hart (2005) are small. As noted earlier, concentrations of Pr to Eu in sample Van7-96-38 are underestimated in our models (Fig. 7). It is possible that the starting mantle for Van7-96-38 is more depleted than D-DMM. Existence of ultra-depleted mantle domains have been proposed for magma genesis beneath mid-ocean ridges based on Os, Nd, and Hf isotope ratios in residual peridotites and olivine-hosted melt inclusions (e.g., Liu et al. 2008; Stracke et al. 2011, 2019; Sanfilippo et al. 2019). The mantle source composition for residual abyssal peridotites such as the ones examined in this study is likely more variable than that represented by the DMM model of Workman and Hart (2005). More study is needed to quantify the abundances of REE and other trace elements in these extremely depleted mantle sources.

Mantle source mode

The starting mantle mode also affects fitting results. Our original purpose of exploring 3–6% variations in cpx and opx modes in the starting lherzolitic mantle was to understand the large variations in mineral modal abundance observed in the mantle xenoliths and abyssal peridotites included in this study, as such variations cannot be produced by melting a single mantle source. It turns out that the quality of fits to the bulk REE in the mantle xenoliths and abyssal peridotites are not very sensitive to the starting mantle mode. This is explained by the very similar bulk REE partition coefficients for the three starting mantle modes: they are subparallel to each other in the spider diagram (see Supplementary Fig. S9). Hence, one cannot use bulk REE in residual peridotite to discriminate starting mantle mode. However, REE abundances in residual cpx and opx are sensitive to starting mantle mode for the mantle xenoliths and abyssal peridotites. This is due to mass balance and temperature-dependent opx/cpx and ol/cpx REE partition coefficients (Eqs. 5, 6). In a closed system (i.e., for a constant C_s in Eq. 5), concentrations of REE in opx and ol in lherzolite or harzburgite decrease with the decrease of temperature, whereas concentrations of REE in cpx increase. At a given temperature, the change of concentration depends on mineral mode (cf. Fig. 2a, b) which, in turn, is sensitive to the starting mantle mode and the melting reaction. With decreasing temperature, cpx and opx modes and major element compositions also change due to pyroxene exsolution and subsolidus reaction among the mantle minerals, which complicates the application of Eq. (6). A preliminary pMELTS-based study suggests that these major element effects are small to moderate on REE redistribution in peridotites (Yao 2015). Results from present study suggest that the mineral mode in the starting mantle is not homogeneous and should be taken into consideration in detailed modeling of REE and other trace elements during mantle melting.

Comparing extent of melting derived from REE in the bulk rock and REE in cpx

In general, degrees of melting based on MCMC inversion of REE + Y in the bulk samples (designated as F_{bulk} hereafter) and cpx alone (F_{cpx}) are positively correlated (Fig. 9). Figure 9a compares our estimated F_{bulk} with F_{cpx} for the nine xenoliths. Samples CK-2 (Coast Ranges of central California, Quinn et al. 2018) and ET80 (East African Rift, Bedini and Bodinier 1999) are considerably more fertile in terms of spinel Cr# and contain 12.4% and 15.8% cpx, respectively. Hence, REE + Y in cpx in these two samples should be less affected by subsolidus redistribution. Indeed, the calculated degrees of melting for CK-2 and ET80 (3.7% and 3.9%) are essentially the same as that derived from HREE in cpx (2.9% and 4.2%, Supplementary Table S2). Nonetheless, light and middle REE in opx in these samples are strongly affected by subsolidus redistribution, which is consistent with their low T_{REE} (964℃ and 952 °C, respectively). The remaining seven xenolith samples are more depleted. Except sample YY-42, their inverted F_{bulk} are 2–6% higher than F_{cpx}.

Sample YY-42 from North China Craton (Liu et al. 2012) has the lowest cpx mode (4%, a harzburgite), the highest spinel Cr#, and the second highest F_{bulk} (19%) among the nine xenolith samples included in this study. This is in contrast to the rather small F_{cpx} for this sample (11%, Table S2). We conclude that the degree of melting inferred from cpx alone in this sample is not meaningful. Caution should be exercised when inferring extent of melting using REE abundance in cpx in harzburgitic mantle xenoliths. This statement also applies to LREE-enriched harzburgites not included in this study, as the inferred degree of melting is based largely on HREE in the peridotites. The latter is less susceptible to mantle metasomatism.

Given the relatively high T_{REE} recorded by the 12 abyssal peridotite samples (Fig. 2) and the limited extent of subsolidus redistribution of REE between cpx and opx (Fig. 7), it is not surprising that the inferred degrees of melting based REE in the bulk samples are only slightly higher than those derived from REE in cpx alone (Fig. 9b). The maximum difference is only 2.2%. Hence, in the absence of bulk REE data, one can use REE in cpx to infer the extent of melting experienced by residual abyssal peridotites.

Variations of extent of melting derived from bulk REE with key melting indices

Chromian spinel has been widely used in studies of abyssal peridotites and peridotites from other tectonic settings (e.g., Dick and Bullen 1984). Hellebrand et al. (2001) showed that spinel Cr# in residual abyssal peridotites are strongly and inversely correlated with HREE abundances in cpx in the peridotites and developed empirical equations relating degree of melting to spinel Cr# for abyssal peridotites. Figure 10a shows the positive correlation between our inverted F_{bulk} and spinel Cr# for the xenolith and abyssal peridotite samples included in this study. The abyssal peridotites are bracketed by the batch melting and perfect fractional melting trends of Hellebrand et al. (2001). However, due to the low spinel Cr#, the mantle xenolith data are mostly plotted below the batch melting trend (open symbols in Fig. 10a). The latter may in part be due to subsolidus redistribution of Cr and Al in spinel peridotite (e.g., Voigt and von der Handt 2011). Caution should be exercised when inferring extent of melting using Cr# of spinel in well-equilibrated mantle xenoliths.

Our inferred degrees of melting for the mantle xenoliths and abyssal peridotites are consistent with the observed variation trends of the major and minor elements in the samples. For example, with increasing degree of melting, MgO in the bulk residue increases from the starting DMM or PM (Fig. 10b), whereas CaO, Al_2O_3, Na_2O, and TiO_2 in the bulk sample decrease (Figs. S2c, S3c). The scatter of the data shown in Figs. 10b, S2c and S3c can be attributed to variations in mineral modes, hence major element composition, in the starting mantle.

Conclusions

LREE-depleted spinel peridotites are generally interpreted as residues of mantle melting. Through case studies of carefully selected residual spinel peridotites from two distinct tectonic settings, we have demonstrated the advantages of using REE abundances in both the bulk rock and constituent minerals (cpx and opx) in deducing magmatic and thermal history of the peridotites. REE abundances in bulk residual peridotites are well suited for studying melting process, provided their concentrations are accurately determined, and grain size and mineral mode are known. As a first application, we kept opx and cpx grain size ratio constant in our MCMC inversion. This is likely a simplification, as we do not know how grain sizes of cpx and opx vary during mantle melting and subsolidus reequilibration. LREE in opx and HREE in cpx are more susceptible to subsolidus redistribution. The extent of redistribution depends on cpx and opx abundances in the sample and thermal history experienced by the peridotite. We have shown that, by modeling subsolidus redistribution of REE between opx and cpx after melting, it is possible to discriminate mineral mode of the starting mantle. HREE in cpx in less primitive spinel lherzolite and harzburgite from subcontinental lithosphere are significantly reset by subsolidus reequilibration over geologic time. We do not recommend the use of REE in cpx alone to study mantle-melting process in such samples. The harzburgite YY-42 from North China Craton (Liu et al. 2012) is an extreme example. In the absence of REE abundance in opx, REE in cpx in residual abyssal peridotites can be used to infer the degree of melting of samples that experienced small to moderate extent of melting. HREE in highly depleted harzburgite may be affected by subsolidus reequilibration. By modeling REE abundances in the bulk and constituent cpx and opx, it is also possible to discriminate starting mantle composition. Results from this study lend support to the common practice of using composition of the primitive mantle to model REE depletion in cratonic mantle xenoliths and composition of DMM to model REE depletion in residual abyssal peridotites. REE patterns in some of the isotopically more depleted abyssal peridotites such as the four samples from SWIR (Warren et al. 2009) can be better explained by a starting mantle that is more depleted than the average DMM.

The mantle xenoliths and residual abyssal peridotites examined in this study are a small fraction of xenolith samples (9 out of 71) and abyssal peridotite samples (12 out of 60) analyzed in the original studies cited in *Case study* 1 and *Case study* 2. To focus on REE depletion in the bulk peridotite produced by partial melting and based largely on

the original studies cited in the two cases, we exclude samples that have LREE-enriched patterns, samples that may have been affected by melt addition, and samples that exhibit disequilibrium partitioning in HREE between opx and cpx. In spite of our conservative approach in sample selection, we find that it is still not possible to reproduce REE + Y patterns in the bulk and pyroxenes in these two groups of highly selective mantle peridotites using a starting mantle with constant mineral mode. It is well known that the upper mantle is chemically (e.g., enriched vs. depleted) and lithologically (e.g., peridotite vs. pyroxenite) heterogenous. Results from the present study suggest that the endmembers of the primitive and depleted peridotitic upper mantle are also modally heterogeneous. A modally heterogeneous mantle source provides a simple explanation for the large variations of mineral mode observed in peridotitic mantle xenoliths and abyssal peridotites. An implication of a modally heterogeneous mantle is that REE abundances of the mantle source (DMM or PM) likely vary with mineral mode, i.e., a modally heterogeneous mantle must also be chemically heterogeneous. A mantle source with constant and uniform composition and mineral mode is merely a convenient starting point in trace element modeling of mantle melting. Although adequate for examining broad variation trends of a suit of peridotitic samples, a uniform mantle source is not sufficient to account for detailed variations of REE in both the bulk peridotite and its constituent minerals, as demonstrated in this study. Given mantle source composition and mineral mode, it is possible to model trace element fractionation during decompression melting of a modally heterogeneous mantle (Liang 2020).

Finally, we note that the methodology developed in this study can also be applied to other trace elements in residual peridotites, provided their diffusion in and partitioning between mantle minerals are well characterized. A potential target is the high field strength elements (HFSE). Spoon- or U-shaped opx/cpx REE partitioning patterns are observed in all the abyssal peridotite samples included in this study. Four of the nine mantle xenoliths that have lower REE closure temperature also exhibit spoon-shaped REE partitioning pattern. Through simple forward modeling, we have shown that the spoon- or U-shaped opx/cpx REE partitioning patterns can be produced by disequilibrium melting followed by diffusive exchange between cpx and opx at subsolidus state. It may be possible to deduce cooling rate and thermal history through detailed modeling of REE and HFSE in coexisting cpx and opx and spoon-shaped opx/cpx REE partitioning patterns in mantle samples. A prerequisite in the subsolidus modeling is the initial concentrations of REE and HFSE in cpx and opx at the onset of cooling which corresponds to the end of the disequilibrium melting modeling. The present study has set a stage for such endeavors in the future.

Appendix: Governing equations and inversion method

The disequilibrium double-porosity melting model of Liang and Liu (2016) is intended for modeling trace element fractionation during concurrent melting, channelized melting extraction, and finite rate of crystal-melt chemical exchange in an upwelling steady-state melting column. In terms of the degree of melting experienced by the solid matrix (F), mass conservation equations for a trace element in the interstitial melt (C_f), residual solid (C_s), individual mineral (C_s^j) can be written as:

$$\varepsilon_{\mathrm{cpx}}(1-\mathbb{R})F\frac{\mathrm{d}C_\mathrm{f}}{\mathrm{d}F}=\varepsilon_{\mathrm{cpx}}\left(C_\mathrm{s}^p-C_\mathrm{f}\right)+\sum_{j=1}^{N}w_j\frac{R_j}{R_{\mathrm{cpx}}}\left(C_\mathrm{s}^j-k_jC_\mathrm{f}\right), \tag{8}$$

$$\varepsilon_{\mathrm{cpx}}(1-F)\frac{\mathrm{d}C_\mathrm{s}}{\mathrm{d}F}=\varepsilon_{\mathrm{cpx}}\left(C_\mathrm{s}-C_\mathrm{s}^p\right)-\sum_{j=1}^{N}w_j\frac{R_j}{R_{\mathrm{cpx}}}\left(C_\mathrm{s}^j-k_jC_\mathrm{f}\right) \tag{9}$$

$$\varepsilon_{\mathrm{cpx}}(1-F)\frac{\mathrm{d}C_\mathrm{s}^j}{\mathrm{d}F}=-\frac{R_j}{R_{\mathrm{cpx}}}\left(C_\mathrm{s}^j-k_jC_\mathrm{f}\right). \tag{10}$$

where k_j is the partition coefficient between mineral j and melt for the element of interest; $\mathbb{R}$ is the dimensionless melt suction rate defined as the fraction of melt removed from the residual solid (to a nearby channel) relative to the amount of melt produced by melting (Iwamori 1994; Liang and Peng 2010); $\varepsilon_{\mathrm{cpx}}$ is the disequilibrium parameter for a trace element in cpx; C_s^p is the concentration of bulk solid calculated according to melting reaction; and w_j is the weight fraction of mineral j in residual solid. The latter three parameters are defined as follows:

$$\varepsilon_{\mathrm{cpx}}=\frac{\Gamma}{\rho_\mathrm{s}\left(1-\phi_\mathrm{f}\right)R_{\mathrm{cpx}}} \tag{11}$$

$$C_\mathrm{s}^p=\sum_{j=1}^{N}w_j^pC_\mathrm{s}^j \tag{12}$$

$$w_j=\frac{w_j^0-w_j^pF}{1-F}, \tag{13}$$

where Γ is the melting rate; ρ_s is the density of the bulk solid; ϕ_f is the volume fraction of the melt in the residue; w_j^0 is the weight fraction of mineral j at the onset of the melting; and w_j^p is the weight fraction of mineral j participating in the melting reaction. Equations (8–10) can be further simplified by assuming that the interstitial melt and olivine and spinel are in local chemical equilibrium. The mass conservation equations become:

$$\left(\varepsilon_{\mathrm{cpx}}(1-\mathbb{R})F+\varepsilon_{\mathrm{cpx}}(1-F)\left(w_{\mathrm{ol}}k_{\mathrm{ol}}+w_{\mathrm{sp}}k_{\mathrm{sp}}\right)\right)\frac{\mathrm{d}C_{\mathrm{f}}}{\mathrm{d}F}$$
$$=\varepsilon_{\mathrm{cpx}}\left(C_{\mathrm{s}}^{p}-C_{\mathrm{f}}\right)+w_{\mathrm{cpx}}\left(C_{\mathrm{s}}^{\mathrm{cpx}}-k_{\mathrm{cpx}}C_{\mathrm{f}}\right)+w_{\mathrm{opx}}\frac{R_{\mathrm{opx}}}{R_{\mathrm{cpx}}}\left(C_{\mathrm{s}}^{\mathrm{opx}}-k_{\mathrm{opx}}C_{\mathrm{f}}\right) \quad (14)$$

$$\varepsilon_{\mathrm{cpx}}(1-F)\frac{\mathrm{d}C_{\mathrm{s}}^{\mathrm{cpx}}}{\mathrm{d}F}=-\left(C_{\mathrm{s}}^{\mathrm{cpx}}-k_{\mathrm{cpx}}C_{\mathrm{f}}\right) \quad (15)$$

$$\varepsilon_{\mathrm{cpx}}(1-F)\frac{\mathrm{d}C_{\mathrm{s}}^{\mathrm{opx}}}{\mathrm{d}F}=-\frac{R_{\mathrm{opx}}}{R_{\mathrm{cpx}}}\left(C_{\mathrm{s}}^{\mathrm{opx}}-k_{\mathrm{opx}}C_{\mathrm{f}}\right) \quad (16)$$

$$C_{\mathrm{s}}^{p}=w_{\mathrm{cpx}}^{p}C_{\mathrm{s}}^{\mathrm{cpx}}+w_{\mathrm{opx}}^{p}C_{\mathrm{s}}^{\mathrm{opx}}+w_{\mathrm{ol}}^{p}k_{\mathrm{ol}}C_{\mathrm{f}}+w_{\mathrm{sp}}^{p}k_{\mathrm{sp}}C_{\mathrm{f}}. \quad (17)$$

Concentration of REE in the bulk residue can be calculated using the expression:

$$C_{\mathrm{s}}=\sum w_{j}C_{\mathrm{s}}^{j}=w_{\mathrm{cpx}}C_{\mathrm{s}}^{\mathrm{cpx}}+w_{\mathrm{opx}}C_{\mathrm{s}}^{\mathrm{opx}}+w_{\mathrm{ol}}k_{\mathrm{ol}}C_{\mathrm{f}}+w_{\mathrm{sp}}k_{\mathrm{sp}}C_{\mathrm{f}}. \quad (18)$$

Equations (14–16) are closed by the following boundary conditions at the bottom of the melting column ($F=0$):

$$C_{\mathrm{f}}(0)=\frac{\varepsilon_{\mathrm{cpx}}k_{p}+k_{0}}{k_{0}\left(\varepsilon_{\mathrm{cpx}}+k_{0}\right)}C_{\mathrm{s}}^{0} \quad (19)$$

$$C_{\mathrm{s}}^{\mathrm{cpx}}(0)=\frac{k_{\mathrm{cpx}}}{k_{0}}C_{\mathrm{s}}^{0} \quad (20)$$

$$C_{\mathrm{s}}^{\mathrm{opx}}(0)=\frac{k_{\mathrm{opx}}}{k_{0}}C_{\mathrm{s}}^{0}. \quad (21)$$

where k_0 is the bulk solid–melt partition coefficient at the onset of melting; and k_p is the bulk solid–melt partition coefficient according to the melting reaction. Equation (19) is based on the analysis of Liang and Liu (2016). Equations (14–16) are a set of coupled ordinary differential equations and can be solved numerically using standard methods.

The disequilibrium double-porosity melting model consists of three coupled nonlinear ordinary differential equations and one algebraic equation for spatial variations of a trace element in interstitial melt, cpx, opx, and bulk residue (Eqs. 14–17). They have no analytical solutions for the problem considered in this study. Hence, we cannot use nonlinear least squares analysis to invert melting parameters as we did for REE in cpx (Liang and Peng 2010; Liang and Liu 2016). To get around this difficulty, we use Markov chain Monte Carlo (MCMC) method to invert the melting parameters F, $\varepsilon_{\mathrm{cpx}}^{1300}$, and $\mathbb{R}$ from REE + Y concentrations in the bulk sample. MCMC methods are a class of powerful statistical tools for solving nonlinear inverse problems in Bayesian analysis (e.g., Sambridge and Mosegaard 2002). Liu and Liang (2017) used MCMC to invert melting parameters from REE abundance in residual cpx in abyssal peridotites. The present work follows the inversion procedure detailed in their study. To facilitate MCMC inversion, we set bounds for the disequilibrium parameter $\varepsilon_{\mathrm{cpx}}^{1300}$ to [0, 0.15] and the melt suction rate $\mathbb{R}$ to [0, 1], based on previous inversion results using similar model or method (Lundstrom 2000; Liang and Peng 2010; Liang and Liu 2016; Liu and Liang 2017). We solve Eqs. (14–21) for each simulation using the routine ODEIENT in Python. We run 10,000–50,000 simulations for each sample to ensure convergence and use the result to calculate best fitting parameters and uncertainties. The best fitting parameters are then used to calculate REE abundances in the bulk sample, residual cpx and opx, and chemically re-equilibrated cpx and opx at closure temperatures in the two pyroxenes.

Supplementary Information The online version contains supplementary material available at https://doi.org/10.1007/s00410-021-01780-x.

Acknowledgements We thank Daniele Brunelli, Henry Dick, Jingao Liu, and Jessica Warren for useful discussion regarding grain size in peridotites, and Suzanne Birner for helpful comments and suggestions on an earlier version of this manuscript. Thoughtful reviews from Daniele Brunelli and Elisabetta Rampone and editorial suggestions from Dante Canil helped to improve the manuscript. This work was supported by National Science Foundation Grant EAR-1852088 and the China Scholarship Council (201806010079).

References

Agranier A, Lee CTA (2007) Quantifying trace element disequilibria in mantle xenoliths and abyssal peridotites. Earth Planet Sci Lett 257:290–298

Anders E, Grevsse N (1989) Abundances of the elements: meteoritic and solar. Geochim Cosmochim Acta 53:197–214

Baker MB, Stolper EM (1994) Determining the composition of high-pressure mantle melts using diamond aggregates. Geochim Cosmochim Acta 58:2811–2827

Bedini R, Bodinier JL (1999) Distribution of incompatible trace elements between the constituents of spinel peridotite xenoliths: ICP–MS data from the East African Rift. Geochim Cosmochim Acta 63:3883–3900

Bodinier J-L, Godard M (2014) Orogenic, ophiolitic, and abyssal peridotites. In: Carlson RW (ed) Treatise on geochemistry: the mantle and core, 2nd edn. Elsevier, New York, pp 103–167

Bodinier JL, Vasseur G, Vernieres J, Dupuy C, Fabries J (1990) Mechanisms of mantle metasomatism: geochemical evidence from the Lherz orogenic peridotite. J Petrol 31:597–628

Brey G, Köhler T (1990) Geothermobarometry in four-phase lherzolites II. New thermobarometers, and practical assessment of existing thermobarometers. J Petrol 31:1353–1378

Brunelli D, Seyler M (2010) Asthenospheric percolation of alkaline melts beneath the St. Paul region (Central Atlantic Ocean). Earth Planet Sci Lett 289:393–405

Brunelli D, Seyler M, Cipriani A, Ottolini L, Bonatti E (2006) Discontinuous melt extraction and weak refertilization of

mantle peridotites at the Vema Lithospheric Section (Mid-Atlantic Ridge). J Petrol 47:745–771
Brunelli D, Paganelli E, Seyler M (2014) Percolation of enriched melts during incremental open-system melting in the spinel field: a REE approach to abyssal peridotites from the Southwest Indian Ridge. Geochim Cosmochim Acta 127:190–203
Cherniak DJ (2015) Nb and Ta diffusion in titanite. Chem Geol 413:44–50
Cherniak DJ, Liang Y (2007) Rare earth element diffusion in natural enstatite. Geochim Cosmochim Acta 71:1324–1340
D'Errico ME, Warren JM, Godard M (2016) Evidence for chemically heterogeneous Arctic mantle beneath the Gakkel Ridge. Geochim Cosmochim Acta 174:291–312
Dick HJB, Bullen T (1984) Chromian spinel as a petrogenetic indicator in abyssal and alpine-type peridotites and spatially associated lavas. Contrib Mineral Petrol 86:54–76
Dygert N, Liang Y (2015) Temperatures and cooling rates recorded in REE in coexisting pyroxenes in ophiolitic and abyssal peridotites. Earth Planet Sci Lett 420:151–161
Elthon D (1992) Chemical trends in abyssal peridotites: refertilization of depleted suboceanic mantle. J Geophys Res 97:9015–9025
Ghiorso MS, Hirschmann MM, Reiners PW, Kress VC (2002) The pMELTS: a revision of MELTS for improved calculation of phase relations and major element partitioning related to partial melting of the mantle to 3 GPa. Geochem Geophys Geosyst 3:1–35
Harvey J, Yoshikawa M, Hammond SJ, Burton KW (2012) Deciphering the trace element characteristics in Kilbourne Hole peridotite xenoliths: melt–rock interaction and metasomatism beneath the Rio Grande Rift, SW USA. J Petrol 53:1709–1742
Hellebrand E, Snow JE, Dick HJB, Hofmann AW (2001) Coupled major and trace elements as indicators of the extent of melting in mid-ocean-ridge peridotites. Nature 410:677–681
Hellebrand E, Snow JE, Hoppe P, Hofmann AW (2002) Garnet-field melting and late-stage refertilization in 'residual' abyssal peridotites from the Central Indian Ridge. J Petrol 43:2305–2338
Hellebrand E, Snow JE, Mostefaoui S, Hoppe P (2005) Trace element distribution between orthopyroxene and clinopyroxene in peridotites from the Gakkel Ridge: a SIMS and NanoSIMS study. Contrib Mineral Petrol 150:486–504
Iwamori H (1994) ^{238}U–^{230}Th–^{226}Ra and ^{235}U–^{231}Pa disequilibria produced by mantle melting with porous and channel flows. Earth Planet Sci Lett 125:1–16
Johnson KTM (1998) Experimental determination of partition coefficients for rare earth and high-field-strength elements between clinopyroxene, garnet, and basaltic melt at high pressures. Contrib Mineral Petrol 133:60–68
Johnson KTM, Dick HJB (1992) Open system melting and temporal and spatial variation of peridotite and basalt at the Atlantis II Fracture Zone. J Geophys Res Solid Earth 97:9219–9241
Johnson KTM, Dick HJB, Shimizu N (1990) Melting in the oceanic upper mantle: an ion microprobe study of diopsides in abyssal peridotites. J Geophys Res Solid Earth 95:2661–2678
Jull M, Kelemen PB, Sims K (2002) Consequences of diffuse and channelled porous melt migration on uranium series disequilibria. Geochim Cosmochim Acta 66:4133–4148
Kelemen PB, Hirth G, Shimizu N, Spiegelman M, Dick HJB (1997) A review of melt migration processes in the adiabatically upwelling mantle beneath oceanic spreading ridges. Philos Trans Math Phys Eng Sci 355:283–318
Key K, Constable S, Liu L, Pommier A (2013) Electrical image of passive mantle upwelling beneath the northern East Pacific Rise. Nature 495:499–502
Kinzler RJ, Grove TL (1992) Primary magmas of mid-ocean ridge basalts 1. Experiments and methods. J Geophys Res Solid Earth 97:6885–6906
Lee CTA, Harbert A, Leeman WP (2007) Extension of lattice strain theory to mineral/mineral rare-earth element partitioning: an approach for assessing disequilibrium and developing internally consistent partition coefficients between olivine, orthopyroxene, clinopyroxene and basaltic melt. Geochim Cosmochim Acta 71:481–496
Liang Y (2003) On the thermo-kinetic consequences of slab melting. Geophys Res Lett 30:2270. https://doi.org/10.1029/2003GL018969
Liang Y (2014) Time scales of diffusive re-equilibration in bi-mineralic systems with and without a fluid or melt phase. Geochim Cosmochim Acta 132:274–287
Liang Y (2020) Trace element fractionation and isotope ratio variation during melting of a spatially distributed and lithologically heterogeneous mantle. Earth Planet Sci Lett 552:116594
Liang Y, Elthon D (1990) Geochemistry and petrology of spinel lherzolite xenoliths from Xalapasco de La Joya, San Luis Potosi, Mexico: partial melting and mantle metasomatism. J Geophys Res 95(15):895–15877
Liang Y, Liu B (2016) Simple models for disequilibrium fractional melting and batch melting with application to REE fractionation in abyssal peridotites. Geochim Cosmochim Acta 173:181–197
Liang Y, Peng Q (2010) Non-modal melting in an upwelling mantle column: steady-state models with applications to REE depletion in abyssal peridotites and the dynamics of melt migration in the mantle. Geochim Cosmochim Acta 74:321–339
Liang Y, Sun C, Yao L (2013) A REE-in-two-pyroxene thermometer for mafic and ultramafic rocks. Geochim Cosmochim Acta 102:246–260
Liu B, Liang Y (2017) An introduction of Markov chain Monte Carlo method to geochemical inverse problems: reading melting parameters from REE abundances in abyssal peridotites. Geochim Cosmochim Acta 203:216–234
Liu B, Liang Y (2019) Importance of permeability and deep channel network on the distribution of melt, fractionation of REE in abyssal peridotites, and U-series disequilibria in basalts beneath mid-ocean ridges: a numerical study using a 2D double-porosity model. Earth Planet Sci Lett 528:115788
Liu C-Z, Snow JE, Hellebrand E, Brugmann G, von der Handt A, Buchl A, Hofmann AW (2008) Ancient, highly heterogeneous mantle beneath Gakkel ridge, Arctic Ocean. Nature 452:311–316
Liu J, Carlson RW, Rudnick RL, Walker RJ, Gao S, Wu F (2012) Comparative Sr–Nd–Hf–Os–Pb isotope systematics of xenolithic peridotites from Yangyuan, North China Craton: additional evidence for a Paleoproterozoic age. Chem Geol 332:1–14
Lundstrom C (2000) Models of U-series disequilibria generation in MORB: the effects of two scales of melt porosity. Phys Earth Planet Inter 121:189–204
McDonough WF, Sun SS (1995) The composition of the Earth. Chem Geol 120:223–253
McDonough WF, Stosch H-G, Ware NG (1992) Distribution of titanium and the rare earth elements between peridotitic minerals. Contrib Mineral Petrol 110:321–328
Navon O, Stolper E (1987) Geochemical consequences of melt percolation: the upper mantle as a chromatographic column. J Geol 95:285–307
Niu Y, Hékinian R (1997) Spreading-rate dependence of the extent of mantle melting beneath ocean ridges. Nature 385:326–329
Quinn DP, Saleeby J, Ducea M, Luffi P, Asimow P (2018) Late-Cretaceous construction of the mantle lithosphere beneath the central California coast revealed by Crystal Knob xenoliths. Geochem Geophys Geosyst 19:3302–3346
Rampone E, Piccardo GB, Vannucci R, Bottazzi P, Ottolini L (1993) Subsolidus reactions monitored by trace element partitioning: the

spinel- to plagioclase-facies transition in mantle peridotites. Contrib Mineral Petrol 115:1–17
Sambridge M, Mosegaard K (2002) Monte Carlo methods in geophysical inverse problems. Rev Geophys 40:1009
Sanfilippo A, Salters V, Tribuzio R, Zanetti A (2019) Role of ancient, ultra-depleted mantle in mid-ocean-ridge magmatism. Earth Planet Sci Lett 511:89–98
Seyler M, Brunelli D, Toplis MJ, Mevel C (2011) Multiscale chemical heterogeneities beneath the eastern Southwest Indian Ridge (52° E–68° E): trace element compositions of along-axis dredged peridotites. Geochem Geophys Geosyst. https://doi.org/10.1029/2011GC003585
Shimizu N (1998) The geochemistry of olivine-hosted melt inclusions in a FAMOUS basalt ALV519-4-1. Phys Earth Planet Inter 107:183–201
Stosch HG (1982) Rare earth element partitioning between minerals from anhydrous spinel peridotite xenoliths. Geochim Cosmochim Acta 46:793–811
Stracke A, Snow JE, Hellebrand E, von der Handt A, Bourdon B, Birbaum K, Günther D (2011) Abyssal peridotite Hf isotopes identify extreme mantle depletion. Earth Planet Sci Lett 308:359–368
Stracke A, Genske F, Berndt J, Koornneef JM (2019) Ubiquitous ultra-depleted domains in Earth's mantle. Nat Geosci 12:851–855
Sun C, Liang Y (2014) An assessment of subsolidus re-equilibration on REE distribution among mantle minerals olivine, orthopyroxene, clinopyroxene, and garnet in peridotites. Chem Geol 372:80–91
Van Orman JA, Grove TL, Shimizu N (2001) Rare earth element diffusion in diopside; influence of temperature, pressure, and ionic radius, and an elastic model for diffusion in silicates. Contrib Mineral Petrol 141:687–703
Van Orman JA, Grove TL, Shimizu N (2002) Diffusive fractionation of trace elements during production and transport of melt in Earth's upper mantle. Earth Planet Sci Lett 198:93–112
Voigt M, von der Handt A (2011) Influence of subsolidus processes on the chromium number in spinel in ultramafic rocks. Contrib Mineral Petrol 162:675–689
Wang C, Liang Y, Xu W (2015) On the significance of temperatures derived from major element and REE based two-pyroxene thermometers for mantle xenoliths from the North China Craton. Lithos 224:101–113
Warren JM (2016) Global variations in abyssal peridotite compositions. Lithos 248:193–219
Warren JM, Shimizu N, Sakaguchi C, Dick HJB, Nakamura E (2009) An assessment of upper mantle heterogeneity based on abyssal peridotite isotopic compositions. J Geophys Res 114:B122023. https://doi.org/10.1029/2008JB006186
Witt-Eickschen G, O'Neill HSC (2005) The effect of temperature on the equilibrium distribution of trace elements between clinopyroxene, orthopyroxene, olivine and spinel in upper mantle peridotite. Chem Geol 221:65–101
Workman RK, Hart SR (2005) Major and trace element composition of the depleted MORB mantle (DMM). Earth Planet Sci Lett 231:53–72
Yang Y, Forsyth DW, Weeraratne DS (2007) Seismic attenuation near the East Pacific Rise and the origin of the low-velocity zone. Earth Planet Sci Lett 258:260–268
Yao L (2015) Closure temperature and closure pressure in bi-mineralic systems with applications to REE-in-two-mineral thermobarometers. Brown University, PhD thesis